34th Symposium on Naval Hydrodynamics
Washington, DC, USA, 26 June - 1 July 2022

Data-Driven Model of the Response of Flexible Hydrofoils in Cloud Cavitation

J. C. Chang[1], S. M. Smith[4], J. A. Venning[4], B. W. Pearce[4], P. A. Brandner[4], Y. L. Young[1,2,3] *

([1]Department of Naval Architecture and Marine Engineering, The University of Michigan, Ann Arbor, MI (USA), [2]Department of Mechanical Engineering, The University of Michigan, Ann Arbor, MI (USA), [3]Department of Aerospace Engineering, The University of Michigan, Ann Arbor, MI (USA), [4]Australian Maritime College, University of Tasmania, Launceston, Australia)

ABSTRACT

The objective of this work is to discover the equations that govern the response of stiff and flexible hydrofoils in cloud cavitation via the usage of Sparse Identification of Nonlinear Dynamics (SINDy). Cavitation is a special form of separated multiphase flow relevant for a diverse range of hydrodynamic lifting bodies such as propellers, flow control surfaces, energy harvesting and energy saving devices that operate at high speeds and/or near the free surface. Since many lifting devices are effectively thin plates or beams subject to high loading, flow-induced deformations and vibrations may occur. The deformations modify the surrounding flow, changing the cavity dynamics and resulting response. In this work, we employ SINDy to discover the coefficients of the nonlinear dynamical system based on experimental data for a stiff stainless steel (SS) and a flexible composite (CF) hydrofoil in cloud cavitation collected at the Australian Maritime College in the Cavitation Research Laboratory water tunnel. We aim to determine the variation of fluid added mass and damping coefficients with the effective cavitation parameter, as well as the resulting fluctuating lift coefficients due to fluid-structure interaction using SINDy, and compare the coefficients with the physics-based reduced-order model (ROM) of the cloud cavitation response of flexible hydrofoils presented in Young et al. (2022).

The results show that in general, while the linear fluid added mass and damping coefficients are approximately the same between the data-driven and physics-based ROM, there were noticeable differences in the trend and magnitude for the nonlinear fluid added mass and damping terms, as well as the rigid hydrofoil cavity forcing terms. Despite these differences, the governing equations with nonlinear damping predicted by SINDy can capture the dominant frequencies of the SS and CF hydrofoils in unsteady cavitating flow. However, the usage of SINDy is limited to the cavitation number range where the intensity of load fluctuations caused by unsteady cloud cavitation is higher than the ambient noise. For this experimental setup, this range is $0.3 \leq \sigma \leq 0.8$. Additional data or more accurate numerical modeling would be needed for proper model development and validation.

INTRODUCTION

Cavitation is a form of separated multiphase flow that commonly occurs on the surface of hydrodynamic lifting surfaces, such as marine propulsors, rudders, energy saving and energy harvesting devices, particularly when the device operates at high speeds and/or near the free surface. Cavitation occurs when the absolute local fluid pressure drops to or slightly below the saturated vapor pressure (Brennen, 1995). The tensile stress that the fluid experiences due to the difference in local pressure and saturated vapor pressure triggers the rupture of the fluid, commonly at voids or small contaminant particles in the fluid, to form vapor bubbles (Brennen, 1995). Sheet cavitation occurs when cavities remain attached to the lifting surface, with a liquid-vapor mixture filling the separated flow region. This work focuses on cloud cavitation, which describes an unsteady or periodic formation, detachment, and collapse of sheet cavities, giving the shed cavities a cloud-like appearance (Brandner et al., 2010).

*Corresponding author, E-mail: ylyoung@umich.edu, Tel.: +1-7346470249.

There are two main driving mechanisms in cloud cavity shedding: re-entrant jet shedding, or Type II shedding, and shock-wave driven shedding, or Type I shedding. Re-entrant jets are formed due to the adverse pressure gradient at the cavity trailing edge, which drives a liquid re-entrant jet beneath the attached sheet cavity. The re-entrant jet flows upstream towards the cavity leading edge to pinch off the sheet cavity at the vapor-liquid interface. The cavity sheds and travels downstream with a cloud-like appearance (Kawanami et al., 1997). This cavity growth and shedding cycle repeats periodically (Pham et al., 1999). The dominant cavity shedding frequency of the re-entrant jet mechanism is dependent on the maximum attached cavity length, and the Strouhal number of the phenomenon lies constant at around 0.2 to 0.4 for different hydrofoil geometries and test conditions (Callenaere et al., 2001). Other cavity shedding frequencies can also be present, as cavities tend to shed in multiple small clouds due to non-uniform cavity length along the span of the hydrofoil caused by 3-D effects (Smith et al., 2020a,b).

The dominant cavity shedding mechanism transitions from re-entrant jet to shock-wave driven shedding when the maximum cavity length is larger than approximately 60% of the body chord length, as the re-entrant jet loses momentum while traveling upstream and becomes unable to pinch off cavities (Fujii et al., 2007; Bhatt et al., 2018; Ganesh et al., 2022). Instead, a shock occurs when the local speed of sound is approximately equal to or lower than the flow speed (Ganesh et al., 2016). The speed of sound through the fluid mixture drops by two orders of magnitude when the local void fraction of the fluid is about 50% to 60% (Shamsborhan et al., 2010). The shock condensation front moves upstream from the trailing edge of the cavity and causes the collapse of the cavities such that the cavities shed periodically at a constant frequency of 10-12 Hz (Fujii et al., 2007; Ganesh et al., 2016; Bhatt et al., 2018; Smith et al., 2020a,b). The re-entrant jet and shock-wave driven cavity shedding mechanisms can both occur at the same time (Smith et al., 2020a,b; Young et al., 2022). An image of shock-wave driven cavity shedding on a hydrofoil can be seen in Figure 1.

Due to the periodic nature of cloud cavitation shedding on hydrodynamic lifting surfaces, and because many lifting devices are effectively flexible thin plates or beams subject to high loading, flow-induced deformations and vibrations may occur. The deformations and vibrations will in turn modify the surrounding flow and change the cavity dynamics and resulting response. This change is known as fluid-structure interaction (FSI). Dynamic vibrations induced by FSI in multiphase flow can result in decreased device performance, controllability, and service life due to fatigue. In addition, changes in the local fluid mixture density and pressure field during unsteady cavitation induce changes in the fluid inertial, damping, and stiffness forces. As a result, hydrodynamic instabilities, such as divergence or flutter, can occur when the total structural and fluid stiffness force or damping force approaches zero, respectively, which increases the system response amplitude (Harwood et al., 2019; Akcabay and Young, 2019, 2020). Changes in inertial and stiffness parameters also induce changes in the system natural frequencies, and may change the order of the mode shapes (De La Torre et al., 2013; Harwood et al., 2020; Young et al., 2020; Ng et al., 2022). The changes in system natural frequencies, as well as the natural variation of Type II shedding frequencies with the effective cavitation parameter can result in lock-in. Lock-in occurs when an external forcing frequency (e.g. cavity shedding frequency) locks into a nearby system natural frequency or its superharmonic/subharmonic. When this occurs, both the cavity shedding frequency and system natural frequency or its harmonic deviate slightly from their original values to synchronize, resulting in dynamic load amplification (Kato et al., 2006; Ausoni et al., 2007; Akcabay et al., 2014; Lelong et al., 2017; Young et al., 2017; Náprstek and Fishcer, 2019). The increased vibrations due to lock-in, instabilities, and resonance can not only cause accelerated fatigue, but also loss of control and failure of the device. As such, understanding and modeling the hydroelastic FSI response in cloud cavitation and other multiphase flows is necessary for the safe and effective operation and control of hydrodynamic lifting surfaces.

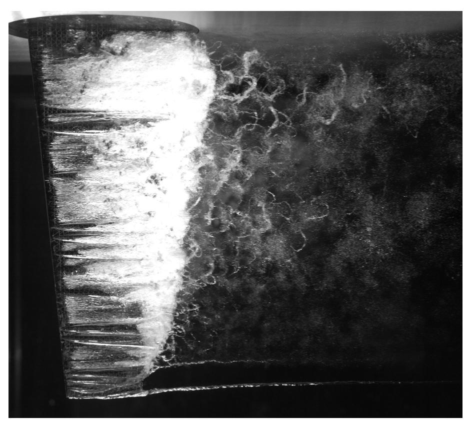

Figure 1: Example image of shock-wave driven cavity shedding on the CF hydrofoil at $\sigma = 0.3$. The cavity length is slightly longer than the chord of the hydrofoil, and the cavitation regime is approaching supercavitation.

Currently, the physics governing flexible lifting devices in cavitation are not well understood. Experimental modeling and data collection is challenging due to many reasons. Firstly, optical collection of data is difficult due to distortion from the changing refractive index of multiphase flows and complications introduced by flow-induced vibrations. Simultaneous collection of data regarding the deforming solid and fluid interface was only recently enabled through shape sensing systems and digital image correlation techniques (Harwood et al., 2019, 2020; Phillips et al., 2017b). Data collection regarding fluid composition of multiphase flow was also recently enabled through x-ray densitometry (Ganesh et al., 2016; Wu et al., 2019). Scaling challenges are also present when working with model-scale experimental data due to the difficulties in meeting all dynamic similarity requirements when working with material and physical limitations under regulatory or testing facility constraints (Ng et al., 2022). Numerical modeling of FSI in multiphase flows is also challenging. Dynamic FSI equations are highly complex and generally require high-fidelity solvers such as a coupled computational fluid dynamics (CFD) and computational structural dynamics (CSD) simulation to resolve. However, a model would need to capture the varying time and length scales of multiphase flow, structural deformations, stress propagations, and resulting FSI to accurately model a system in multiphase flow. Moreover, there is currently no reliable numerical model to capture this phenomenon. Thus, this work focuses on developing a data-driven, low-fidelity model that can accurately model the dynamic FSI response of flexible lifting surfaces in cloud cavitation. The model must be based on physics to abide by known conservation laws and to ensure explainability and scalability. However, because the knowledge of the physics is currently limited, it is important to develop the model based on data to correct for invalid assumptions. For example, viscous FSI effects, such as changes in tip vortices and shed vortex dynamics caused by flow-induced bending and twisting deformations, may not be negligible. In this case, the potential flow assumption would not be valid.

Due to the availability of data and the computational resources to store and process the data, many fields of studies are building data-driven models to predict responses that were previously unknown. In addition, low-fidelity models are on the rise due to the significant computational savings they offer when compared to traditional CFD/CSD and other high-fidelity solvers, which opens the doors for applications such as real-time fluid flow and structural health monitoring and control, as well as rapid surveying of large design spaces. This interest is also true in the maritime and aerospace industries, where data-driven reduced-order models (ROMs) are being built to model various flow conditions (Akcabay and Young, 2015; Gao et al., 2017; Stabile et al., 2018; Alavi et al., 2018; Young et al., 2022). However, many challenges exist when building data-driven models. First, real world data sets contain noise due to sensor functions, external events, or other sources, which can bias the data or result in overfitting of the model. Second, the scope of the collected data is often limited, as it can be difficult to collect data for the number of cycles needed to obtain sufficient statistics or collect data during unstable responses. The lack of data can result in a model with only limited accuracy under certain operating conditions. Finally, unless some physics is known, data-driven models would be near impossible to scale between model- and full-size structures.

To combat the above challenges, the Sparse Identification of Nonlinear Dynamics (SINDy) was introduced as an algorithm to discover governing equations of unknown systems from data (Brunton et al., 2016). SINDy works by assuming that the derivatives of the state variables of a system are related to a sparse nonlinear combination of the state variables. As such, it intakes a library of candidate functions, and performs a regression with the data to determine the coefficients on each function. To promote sparsity, a coefficient magnitude threshold is enforced, and the terms with coefficients that do not meet this threshold are dropped. The process is repeated until a sufficiently sparse and accurate model is obtained. SINDy is highly sensitive to data processing. It may have difficulties when two functions give similar state behaviors and may rely on the transient response to differentiate between functions. However, the transient response may not always be available. The process also requires the derivative of state variables, which is usually not measured. Because physical data always contain noise, and the differentiation process amplifies noise, the model identification can be skewed. However, SINDy is powerful in that while a library of candidate functions needs to be chosen, no set equation form needs to be assumed prior to the identification process. Additionally, when the library of candidate functions is small, the identification process is computationally efficient even with nonlinear terms.

The main contribution of this work is the development of a reduced-order, nonlinear model using SINDy that improves upon the reduced-order model (ROM) of Young et al. (2022). This would further illuminate the physics governing FSI in multiphase flows, including the variation of fluid added mass and damping in time and with the effective cavitation parameter.

METHODOLOGY

Experimental Methods

Model Setup and Hydrofoil Geometry - The experimental setup and techniques of this investigation were completed in the Cavitation Research Laboratory water tunnel of the Australian Maritime College. Brandner et al. (2007) presented a thorough description of the facility. The flow conditions in the Cavitation Research Laboratory were set at a constant chord-based Reynolds number $Re = U_\infty c/\nu$ of 0.8×10^6, where U_∞ is the freestream velocity, c is the mean chord, and ν is the kinematic viscosity. The cavitation number is defined as $\sigma = 2(p_\infty - p_v)/(\rho_f U_\infty^2)$, where p_∞ is the absolute static pressure at the hydrofoil tip, p_v is the vapor pressure, and ρ_f is the water density. The cavitation number was systematically lowered from 1.2 to 0.2 to cover cavitation regimes ranging from partial leading edge sheet cavitation to supercavitation. The dissolved oxygen levels of the fluid were maintained at 3 to 4 ppm for all measurements.

Two hydrofoils with the same undeformed geometry were tested. One hydrofoil was made of Type 316 stainless steel (SS hydrofoil), and the other was made of a carbon/glass-epoxy hybrid composite (CF hydrofoil). The hydrofoils have a span of s = 300 mm, a root chord of c_{max} = 120 mm, a tip chord of c_{min} = 60 mm, and a mean chord c of 90 mm. The planform is unswept and linearly tapered. The cross sections of the hydrofoils are a modified NACA0009 section, with the trailing edge thickened to accommodate the composite layup. Details of the section can be found in Zarruk et al. (2014). The details of the manufacturing can be found in Smith et al. (2020a) and Smith et al. (2020b) for the SS and CF hydrofoils, respectively. The hydrofoils were mounted at an initial angle of attack of 6°, and further details of the mounting setup, instrumentation details, test procedures, and results can be found in Smith et al. (2020a). The basic material properties of the hydrofoils can be found in Table 1. Note that $f_{n1,dry}$ and $f_{n1,FW}$ denote the in-air and in-water fully wetted (FW) fundamental (bending) natural frequencies, respectively. The resonance frequencies are lower when fully wetted due to the higher fluid inertial (added mass) effect. The modal frequencies tend to increase with increasing extent of cavitation due to reduced fluid added mass as more water is replaced with vapor on the suction side, which has been explained in Young et al. (2022).

The hydrofoils were selected to explore the influence of flexibility, so they were built to have matching undeformed geometries and quasi-isotropic properties. Due to these considerations and the material composition of the two hydrofoils, the SS and CF hydrofoils have different natural frequencies. The difference in natural frequencies allows for exploration of the differences in hydrofoil responses that arise, such as lock-in of the cavity shedding frequency with different subharmonics of the natural frequency. The influence of the different resonance frequencies can be found in Young et al. (2022), and discussions of scaling effects can be found in Ng et al. (2022).

Table 1: Material and structural properties of the SS and CF hydrofoils (Zarruk et al., 2014).

Hydrofoil	SS (Stiff)	CF (Flexible)
E (GPa)	193	65
G (GPa)	77.2	22
I (mm^4)	6,148	6,148
J (mm$^4 \times 10^3$)	854.5	854.5
ρ_s (kg/m^3)	7,900	1,600
ρ_s/ρ_f	7.9	1.6
K_s (kN/m)	200	69
M_s (kg)	0.577	0.117
$f_{n1,dry}$ (Hz)	94	121
$f_{n1,FW}$ (Hz)	58	41

Measurement and Data Processing Techniques -
Measurements were collected in three different run types, labeled Long, Medium, and Short. The details of the run types are summarized in Table 2. Force measurements were taken during all three run types. Due to memory limitations, image data was only taken during the Medium and Short run types. The normal force was measured by a force balance. The tip deflection was measured using a Phantom v2640 high speed camera with a Nikkor 105mm f/2.8G lens. The pixel resolution was 512 × 1504 for the SS hydrofoil and 896 × 1504 for the CF hydrofoil. The spatial resolution was 0.049 mm px^{-1} for both hydrofoils. The tip deflection was calculated through an edge detection process by identifying peaks in the pixel intensity gradient along each row of pixels. The tip bending displacement, δ, was determined by taking the average distance of every row after the twisting deformation was removed. Positive δ is defined as translation towards the suction side.

Table 2: Data collection details of the various run types, with the run duration, T, high-speed photography frame rate, f_{HSP} and force balance sampling rate, f_{FBS}.

Run Type	T (s)	f_{HSP} (Hz)	f_{FBS} (Hz)
Long	360	N/A	1,000
Medium	36	500	500
Short	1	6,600	6,600

One Degree-of-Freedom Dynamic ROM

This section briefly summarizes the one degree-of-freedom (1-DOF) ROM presented for tip bending displacement in Young et al. (2022). The SS and CF hydrofoils are assumed to be quasi-isotropic and linearly elastic, to undergo negligible chordwise deformation, and to have no material bend-twist coupling. Because the FW bending and twisting modal frequencies of the hydrofoils are well separated, the bending and twisting degrees of freedom can be assumed to be uncoupled, and the 1-DOF model is valid for simulating only the bending fluctuations of the hydrofoils. The focus is on the cavity-induced fluctuations of the bending displacement and normal force, which are earlier indicators of cavitation inception when compared to the steady deformations and loads, as observed in Young et al. (2022). Moreover, the frequency response of the fluctuations yields information about cavity shedding mechanisms and hydrofoil vibration characteristics, as observed in the data presented in Smith et al. (2020a,b); Young et al. (2022).

While twisting deformations were present, the results presented in Smith et al. (2020a,b); Young et al. (2022) showed that the twisting deformations were very small. The CF hydrofoil underwent a maximum mean tip twist of about 0.8° in FW conditions at an initial angle of attack of 6° (Smith et al., 2020b; Young et al., 2022). The corresponding maximum mean tip twist of the SS hydrofoil was less than 0.1°, and the twisting measurements for the SS hydrofoil were not clearly resolved with the precision of the method of data acquisition (Smith et al., 2020a; Young et al., 2022). The effect of the mean tip twist was included in the model via the usage of the effective cavitation parameter, as defined in Equation 8. The focus of the paper is to capture the dynamic, or fluctuating response, of the bending deformations, which is obtained by subtracting the mean values from the total deformation. The twisting resonance frequencies of the hydrofoils in water (255 Hz for the SS hydrofoil and 179 Hz for the CF hydrofoil) were much higher than that of the bending resonance frequencies (58 Hz for the SS hydrofoil and 41 Hz for the CF hydrofoil) and higher than that of the force balance resonance frequency (122 Hz) (Young et al., 2022). Since the resonance frequencies of the two modes are well separated, and the higher frequency response could be contaminated by the excitation of the force balance, only the bending fluctuations were considered, and a bandpass filter was used to process the data.

The tip bending fluctuations (δ') were determined by subtracting the mean tip bending (δ) from the instantaneous tip bending displacement ($\tilde{\delta}$):

$$\delta' = \tilde{\delta} - \delta \tag{1}$$

Therefore, the equation of motion for the bending fluctuations is written as below:

$$M_s\ddot{\delta}' + C_s\dot{\delta}' + K_s\delta' = F_N' \tag{2}$$

Here, M_s and C_s are the effective structural mass and damping, respectively. K_s is the effective structural stiffness. Experimental measurements of the structural damping coefficients of metallic and composite hydrofoils were found to be over an order of magnitude lower than the FW damping coefficients for the first bending mode (Blake and Maga, 1975; Phillips et al., 2017a; Harwood et al., 2020). Hence, C_s is assumed to be zero for the sake of simplicity.

F_N', or the fluctuating normal hydrodynamic force, can then be separated into two components: the unsteady cavity shedding force fluctuation on an equivalent rigid hydrofoil component, F_R', and the FSI component, F_{FSI}' such that:

$$F_N' = F_R' + F_{FSI}' = C_N' qsc \tag{3}$$

$$F_{FSI}' = -\left(\hat{M}_f\ddot{\delta}' + C_f\dot{\delta}' + K_f\delta'\right) \tag{4}$$

In these equations, $\hat{M}_f$, C_f, and K_f are the fluid inertial, damping, and disturbing force terms. They relate to the fluctuating bending acceleration, velocity, and displacement, respectively. C_N' is the fluctuating normal force coefficient corresponding to the normal hydrodynamic force, and $q = 0.5\rho_f U_\infty^2$ is the dynamic pressure.

By moving the FSI forces to the left-hand side, Equation 2 can be rewritten as follows:

$$\left(M_s + \hat{M}_f\right)\ddot{\delta}' + \left(C_s + C_f\right)\dot{\delta}' + \left(K_s + K_f\right)\delta' = F_R' \tag{5}$$

Since only the bending DOF is considered, $K_f = 0$. In potential flow, pure bending or heave displacement perpendicular to the flow does not influence the normal force on the body.

The fluctuating normal force due to unsteady cavity shedding on a rigid hydrofoil can be modeled as simple sinusoidal oscillations at the cavity shedding frequencies:

$$F_R' = F_{Ro}'\left[\sin(2\pi f_{c1}t + \phi_1(t)) + \sin(2\pi f_{c2}t + \phi_2(t))\right] = C_R' qsc \tag{6}$$

where f_{c1} and f_{c2} are the Type I shock-wave driven and Type II re-entrant jet driven cavity shedding frequencies, respectively. ϕ_1 and ϕ_2 are random phase variations between 0 and π. C_R' is the fluctuating normal force coefficient for an equivalent rigid hydrofoil.

The amplitude of the normal force coefficient, C'_{Ro}, is modeled as follows:

$$C'_{Ro} = \frac{F'_{Ro}}{qsc} = \frac{1}{15}\exp\left(-0.7(\psi_e - 2.8)^2\right) \tag{7}$$

ψ_e is the effective cavitation parameter, calculated as follows:

$$\psi_e = \sigma/(2\alpha_e) \tag{8}$$

The effective cavitation parameter is dependent on the effective angle of attack, $\alpha_e = \alpha_0 + S_g\theta$, where $S_g = 1/3$ is the integral of the twist shape function of the hydrofoil, which is presented in Young et al. (2022), and θ is the mean tip twist. Using α_e accounts for differences in the mean tip twist between the SS and CF hydrofoils. It can be seen that $C'_{Ro} \to 0$ for $\psi_e \to \infty$ and $C'_{Ro} \sim 0$ for $\psi_e = 0$. This follows the physics in that the fluctuations decay to zero in stable fully wetted flow and in stable supercavitating flow. Since the fluctuating normal force amplitude depends on the extent of cavitation, ψ_e is used in Equation 7. Equation 7 gives the fluctuating normal force coefficient for an equivalent rigid hydrofoil, and is obtained by curve fitting the measured standard deviation of the fluctuating normal force induced by unsteady cavity shedding for the SS hydrofoil.

As found in previous literature, the Type I shock-wave driven cavity shedding frequency is between 10-12 Hz and varies approximately linearly with the effective cavitation parameter over a limited cavitation parameter range, where the maximum attached cavity length is approximately 60% to 120 % of the chord length:

$$f_{c1} = 10 + \frac{(\psi_e - 0.9)}{1.2}\ \text{Hz} \quad \text{for} \quad 0.9 \le \psi_e \le 3.3 \tag{9}$$

As noted in the Introduction, re-entrant jet and shock-wave driven cavity shedding can occur simultaneously at a given cavitation number, either in different portions of the span or interacting. The different cavity shedding mechanisms can occur at different random phases. Thus, ϕ_1 and ϕ_2 are included in Equation 6.

Type I cavity shedding occurs over a limited range of the effective cavitation parameter ($0.9 \le \psi_e \le 3.3$), where the void fraction is in the proper range for decreased local speed of sound. For $\psi_e > 3.3$, when the maximum cavity length is less than 60% of the chord length, only Type II cavity shedding is present, so Equation 6 reduces to $F'_R = F'_{Ro}\sin(2\pi f_{c2}t + \phi_2)$.

Young et al. (2022) fitted the experimental results from Smith et al. (2020a,b) to relate the Type II re-entrant jet driven cavity shedding frequency to ψ_e:

$$St_2 = \frac{f_{c2}c}{U_\infty} = 0.0045\psi_e^3 + 0.12 \tag{10}$$

ψ_e is used in both Equations 9 and 10 to account for the effective angle of attack, α_e, with consideration for the flow-induced mean tip twist, which is more significant for the CF hydrofoil than the SS hydrofoil.

The fluid added mass, $\hat{M}_f$, oscillates with the periodic shedding of the cavity due to changes in the local fluid mixture density. $\hat{M}_f$ is assumed to be modulated by the Type II re-entrant jet cavity shedding frequency only in Young et al. (2022):

$$\hat{M}_f(t) = M_f\left[1 + \varepsilon_m \sin(2\pi f_{c2}t)\right] \tag{11}$$

$$M_f = \frac{M_f^{FW}}{1 - \varepsilon_m} \tag{12}$$

$$\varepsilon_m = \frac{1}{6}\left[\tanh(\psi_e - 3.4) - 1\right] \tag{13}$$

M_f is the effective mean fluid added mass in bending. $M_f^{FW} = f_{mf}\pi\rho_f c^2 s/4$ is the effective fluid added mass in FW flow. $f_{mf} = 0.47$ is the constant bending shape factor for both hydrofoils, as the two hydrofoils share the same undeformed geometry. The maximum value of $\hat{M}_f$ corresponds to the fully wetted value, i.e. $M_{f,max} = M_f^{FW}$, while the minimum value of $\hat{M}_f$ decreases with decreasing effective cavitation parameter ψ_e, as the cavity length increases and lighter vapor takes the place of liquid. The minimum value of $\hat{M}_f$ corresponds to the supercavitation regime in which the entire suction side of the hydrofoil is enveloped by the vaporous cavity, or $M_{f,min} \to 0.5M_f^{FW}$.

The wetted system natural frequency in bending, f_{n1}, is a function of the structural stiffness, K_s, and structural and fluid added mass, M_s and $\hat{M}_f(t)$. The wetted natural frequency can be obtained by solving the eigenvalue problem of Equation 5. It is fluctuating due to the time-varying fluid added mass, and given in the following equation:

$$\hat{f}_{n1} = \sqrt{\frac{K_s}{(M_s + \hat{M}_f)}} \tag{14}$$

The fluid damping coefficient, ζ_f, is calculated as a linear function of the mean system bending frequency, ignoring the fluctuations. Referencing Blake and Maga (1975), the fluid damping coefficient is calculated assuming a nearly 2-D response using Equation 15:

$$\zeta_f = \frac{C_s + C_f}{2\sqrt{(M_s + M_f)K_s}} = \frac{U_\infty}{2f_{n1}c} \tag{15}$$

Due to the negligible structural damping, the fluid damping coefficient, ζ_f, composes the total damping. The mean fluid added mass, M_f, and the mean system bending frequency, f_{n1}, are used when computing the damping coefficient with Equation 15, because the oscillations due to cavitation are assumed to be small.

SINDy Problem Formulation

SINDy Algorithm - As developed by Brunton et al. (2016), SINDy assumes that the derivative of the state variables is a sparse nonlinear function of the state variables, as shown below:

$$\frac{d}{dt}x(t) = f(x(t)) \tag{16}$$

$x(t) \in \mathbb{R}^n$ denotes the state of a system at time t, and $f(x(t))$ denotes the relationship between $x(t)$ and its derivative, which can generally be found through the equations of motion. Thus, the SINDy algorithm works with Equation 17:

$$\dot{X} = \Theta(X)\Xi \tag{17}$$

Here, X is the data taken regarding the system states, organized in column form, $\dot{X}$ is its derivative, and Θ is a library of candidate functions to be identified, such as polynomials of trigonometric functions, applied to the state X. Each column of Θ corresponds to one candidate function. Ξ is a matrix which holds the coefficients of the various candidate functions. Ξ can be determined by a least squares regression, but to enforce sparsity, a simple threshold is maintained for the coefficients such that candidate functions with low values for the coefficients are dropped. The process is repeated until sparsity is achieved.

SINDy Application - Due to the nature of the data collected in this experiment, we have made slight modifications to the applications of the SINDy algorithm.

Knowing that we measured the fluctuating normal force (F_N'), we can make some assumptions regarding the rigid hydrofoil fluctuating normal force. We can assume that F_R' takes the form of two sine waves with random phase shifts, such as in Equation 6, where F_R' is presented as the sum of one or two sine waves at the cavity shedding frequencies. We can also assume F_{FSI}' to have linear and sinusoidal damping and added mass components, corresponding to the FW and the cavity-induced fluctuating components, respectively. The fluid disturbing force is assumed to be negligible compared to the hydrofoil structural stiffness, thus $K_f \approx 0$.

The expected coefficients would differ by two orders of magnitude in the dimensional equation, which would bring difficulties when setting a coefficient threshold. As such, the equation is normalized as below:

$$\bar{F}_N' = \frac{F_N'}{0.5\rho_f s c^3 \omega_{n1,dry}^2} = \frac{f(\delta', \dot{\delta}', \ddot{\delta}')}{0.5\rho_f s c^3 \omega_{n1,dry}^2} \tag{18}$$

For clarity, an overhead bar is used to denote nondimensional values. As examples, $\delta'/c = \bar{\delta}'$, $\dot{\delta}'/(c\omega_{n1,dry}) = \bar{\dot{\delta}}'$, and $\ddot{\delta}'/(c\omega_{n1,dry}^2) = \bar{\ddot{\delta}}'$. The least squares identification is set up in the following manner:

$$\bar{F}_N' = \Theta(\bar{\dot{\delta}}', \bar{\ddot{\delta}}')\Xi \tag{19}$$

$$\Theta(\bar{\dot{\delta}}', \bar{\ddot{\delta}}') = \begin{bmatrix} - & \bar{\dot{\delta}}' & - \\ - & \bar{\ddot{\delta}}' & - \\ - & \bar{\dot{\delta}}'\sin(2\pi f_{c2}t) & - \\ - & \bar{\dot{\delta}}'\cos(2\pi f_{c2}t) & - \\ - & \bar{\ddot{\delta}}'\sin(2\pi f_{c2}t) & - \\ - & \bar{\ddot{\delta}}'\cos(2\pi f_{c2}t) & - \\ - & \sin(2\pi f_{c2}t) & - \\ - & \cos(2\pi f_{c2}t) & - \\ - & \sin(2\pi f_{c1}t) & - \\ - & \cos(2\pi f_{c1}t) & - \end{bmatrix}^T \tag{20}$$

Equation 20 shows the function library used during the identification process. The rigid hydrofoil fluctuating normal force (F_R') is assumed to be a sum of sinusoidal functions oscillating at the cavity shedding frequencies, and is encompassed by the last four columns of the function library. The top six columns of the function library are assumed to be related to F_{FSI}'. To identify the effects of the periodic cavity shedding on fluid added mass and damping, sinusoidal terms related to the tip bending velocity and acceleration are included at the Type II cavity shedding frequency. The Type I cavity shedding frequency is not considered because its effects are much smaller than those of the Type II cavity shedding frequency, as assumed in Young et al. (2022). We chose to only include candidate functions that are informed by physics, because when many candidate functions are included, some functions may be similar in the range of interest, making identification difficult. Both sine and cosine terms are included for each sinusoidal related term to account for a random phase shift caused by the stochasticity of the cavity shedding. Assuming that the periodic forcing occurs at a given frequency but a random phase, a sine term can be separated to a sine and cosine term as shown below:

$$A\sin(\omega t + \gamma) = B\sin(\omega t) + C\cos(\omega t) \tag{21}$$

$$A = \sqrt{B^2 + C^2} \tag{22}$$

During the identification process, the equivalent of B and C are calculated, and magnitude, A, for the sinusoidal components of the candidate functions shown in Equation 20 is presented in Figures 5, 6 and 7. The phase is not presented because it is random due to the stochasticity of cavity shedding. Because Type I cavity shedding does not occur at all cavitation numbers, forcing at the corresponding frequency is only included when present. When not present, Θ drops the last two columns.

Although data was available for additional cavitation numbers, SINDy was only performed for $0.3 \leq \sigma \leq 0.8$. The identification was not performed because at $\sigma < 0.3$, the stable supercavitation regime occurs; at $\sigma > 0.8$, small partially attached sheet cavities occur. There is no significant forcing and displacement fluctuation signal to analyze, as any fluctuation is on a similar order of magnitude as noise. The cavity shedding on the CF hydrofoil at $\sigma = 0.3$ and $\sigma = 0.8$ can be observed in Figures 1 and 2, respectively.

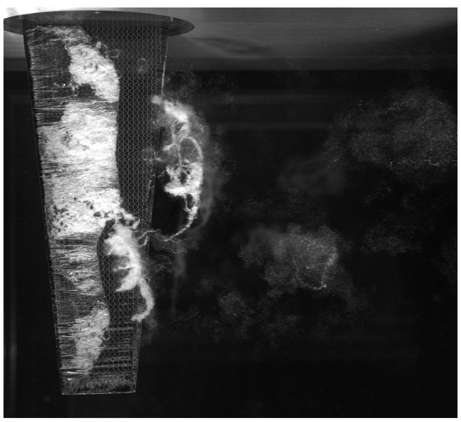

Figure 2: Example image of cavity shedding on the CF hydrofoil at $\sigma = 0.8$. The cavity length is approximately half of the chord of the hydrofoil, and clear cloud cavitation with the re-entrant jet driven cavity shedding mechanism can be observed.

Only displacement data was collected during the experiment, and the differentiation of data, particularly polychromatic data, as in this case, amplifies noise and is highly influential during identification. $\dot{\bar{\delta}}'$ and $\ddot{\bar{\delta}}'$ were calculated using the `smooth_diff` function in MATLAB using a filter length of 2 (Luo, 2022). To remove noise induced from numerical differentiation, a bandpass filter with a minimum frequency of 1 Hz and a maximum frequency of 50 Hz was applied to the velocity series and acceleration series after the calculation. Both data sets were also detrended to remove the mean component of the velocity and acceleration. The differentiation for $\ddot{\bar{\delta}}'$ was completed after the filtering of $\dot{\bar{\delta}}'$. To further smooth out the data, after the nonlinear time series in Θ were assembled, each column in Θ was numerically integrated through the trapezoidal method twice, as the data sets were differentiated twice to retrieve the acceleration. Integration smooths out the data, particularly at higher frequencies. Between each integration, the moving average of the time series resulting from numerical integration was removed with a window of 85 data points, which corresponds to 0.5% of the data points within each time series. After the coefficients were identified with the SINDy algorithm, the coefficients were fitted to develop a data-driven model. The model was applied to the collected displacement data and derived velocity and acceleration data to calculate the total forcing, F_N', and the results are compared against the experimental data.

The SINDy identification process, excluding any pre- and post-processing of the data, required an average CPU time of 0.0923s for $\Theta \in \mathbb{R}^{17000\times 10}$ and 0.0677s for $\Theta \in \mathbb{R}^{17000\times 8}$ on an Intel(R) Xeon(R) CPU E3-1246 v3 at 3.50GHz with 16.0GB RAM.

RESULTS

The coefficients for each candidate function returned by SINDy in dimensional form is shown below, along with comparisons to the values used in the ROM from Young et al. (2022) summarized in the Methodology section. Figures 3 and 4 show the linear coefficients, corresponding to the first two columns of Equation 20, which are the velocity (damping force) and acceleration (inertial force) of the SS and CF hydrofoils, respectively. For each oscillating forcing term, both the sine and cosine terms were included in Θ to account for phase variations. Figures 5 and 6 show the amplitude of the sine and cosine coefficients as calculated by Equation 22, while the phase is not shown, as it is random. Figure 7 shows the SINDy estimated values for C_{Ro}', corresponding to the last four columns of Equation 20, with the fit considering both oscillations at f_{c1} and f_{c2}. The coefficients are plotted to the effective cavitation parameter, ψ_e, instead of cavitation number, σ, to account for differences that occur due to the higher twist deformation of the CF hydrofoil. Expressing the results in ψ_e also allows the model to be applicable for any σ and α_e combination. The fit of the SINDy predicted values are also shown in the figures, and will be discussed later when presenting the data-driven model derived from the identification. A few coefficients lie off the range of the plots, and are considered outliers.

When looking at Figures 3 and 4, the coefficients estimated by SINDy appear to be in the same order of magnitude as the ROM presented in Young et al. (2022) for both the SS and CF hydrofoils. Some coefficients estimated for the SS hydrofoil appear to be higher than the ROM values, but the difference is within one order of magnitude. The discrepancy between the predicted coefficients for the SS and CF hydrofoils is likely due to the difference in uncertainty and signal-to-noise ratio of the displacement data between the two hydrofoils. Since both the SS and CF hydrofoils share the same undeformed geometry, the fluid added mass coefficients should be the same for both hydrofoils and independent of the hydrofoil material properties, while the fluid damping would differ due to the different wetted natural frequencies of the system, as shown in Equation 15. This was the logic used when formulating the ROM in Young et al. (2022). However, because the data processing and experimental methods are the same between the two hydrofoils, it is reasonable to assume the magnitude of the noise is the same between the measurements taken on the two hydrofoils. Since the SS hydrofoil undergoes lower bending deformation due to its higher stiffness, the SS hydrofoil data would have a lower signal-to-noise ratio than the CF hydrofoil data. Some coefficients estimated by SINDy were also negative, which is unexpected, but can be attributed to the function of the algorithm, which will be summarized later.

It can be seen in Figures 5 and 6 that the magnitude of the sinusoidal oscillation of fluid added mass and damping are often active at the Type II cavity shedding frequency. The oscillation amplitudes are about the same between the two hydrofoils, and in the same order of magnitude but slightly lower than the mean values shown in Figures 3 and 4. The fits of the sinusoidal oscillation amplitude are constrained to approach a value close to 0 for $\psi_e > 4$ because stable fully wetted flow is observed at high effective cavitation parameters. The fits are also constrained to approach a value close to 0 for $\psi_e < 1$, as stable supercavitation is observed at low effective cavitation parameters. Considering the physics, the amplitude of fluid added mass and damping oscillations should also be equal between the two hydrofoils, since they have the same undeformed geometry, and thus the fit is assumed to be the same between the two hydrofoils.

Figure 7 shows that the identified C'_{Ro} is about an order of magnitude smaller than predicted in Equation 7. However, it is unlikely that such a low rigid hydrofoil forcing can cause the levels of displacement observed on the hydrofoil. This discrepancy may be attributed to the inaccuracy of the assumed form of rigid hydrofoil forcing. While the forcing is expected to be periodic, it may not be sinusoidal. In addition, the random time-varying phase associated with the forcing is not known, and therefore an accurate basis could not be formed to be considered as a candidate function for SINDy.

There are a few limitations of the SINDy algorithm that can cause the unexpected coefficient predictions. SINDy was used on each data set independently, thus there is no consideration for continuity of trends based on the effective cavitation parameter during the identification process. In addition, SINDy operates using a least squares fit, and therefore scales each candidate function such that the sum of the square of the error between each corresponding point in the time histories of the identified C'_N and measured C'_N is at its minimum. However, this does not guarantee that the error between the coefficients of each term in the governing equation is minimal when noise is present. In addition, the current SINDy algorithm is unable to predict time-varying phase angles. SINDy utilizes the multiple measurements of data points in time to identify coefficients, assuming constant phase. These issues may be a cause of the difference in amplitude between the identified C'_{Ro} and Equation 7, as well as identification errors that result in negative coefficients in Figures 3 and 4, where the coefficients are expected to be positive.

After the development of the fitted data-driven model, the fitted curves in Figures 3 through 7 were applied to the displacement, velocity, and acceleration data to calculate the fluctuating normal force coefficient (C'_N, as defined in Equations 3 and 4) to visualize the accuracy of the model. The resulting power spectral densities (PSDs) of measured C'_N are shown in Figure 8, and the PSDs of C'_N of the SINDy data-driven model are shown in Figure 9.

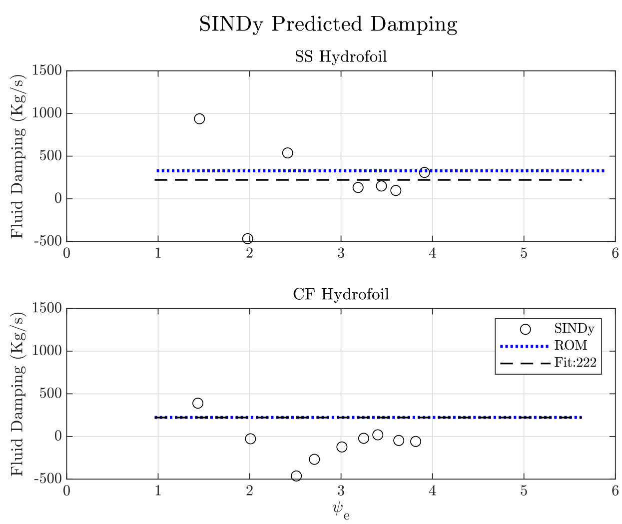

Figure 3: SINDy predicted coefficients of the linear fluid damping compared to ROM values developed by Young et al. (2022). The top and bottom plots show the results for the SS and CF hydrofoils, respectively. The fit of the SINDy predicted value is shown by the black dashed line. Values predicted by SINDy are in the same order of magnitude compared to the ROM values.

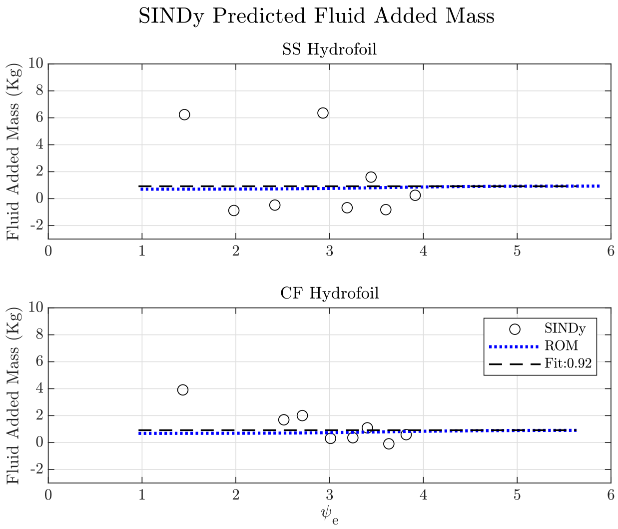

Figure 4: SINDy predicted coefficients of the linear fluid added mass compared to ROM values developed by Young et al. (2022). The top and bottom plots show the results for the SS and CF hydrofoils, respectively. The fit of the SINDy predicted value is shown by the black dashed line. Values predicted by SINDy are in the same order of magnitude compared to the ROM values.

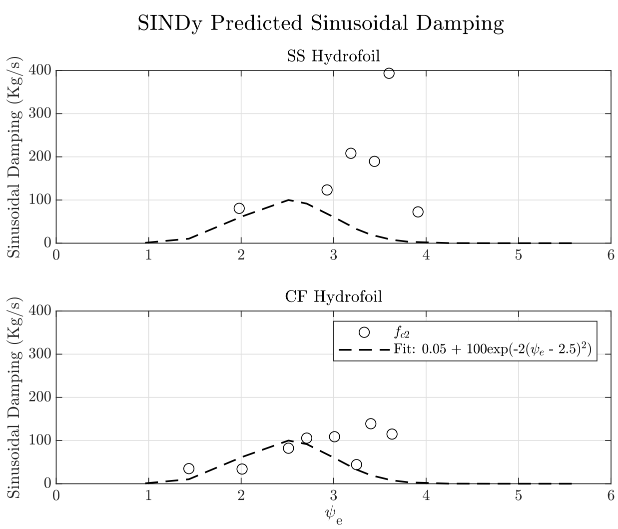

Figure 5: SINDy predicted coefficients of the time-varying sinusoidal fluid damping. The open black circles denote the amplitudes (square root of the sum of the squares) of the sine and cosine terms in Equation 20 at the Type II cavity shedding frequency. The fit is shown by the black dashed line. Values predicted by SINDy show that time-varying fluid damping is significant in the fluid-structure interaction.

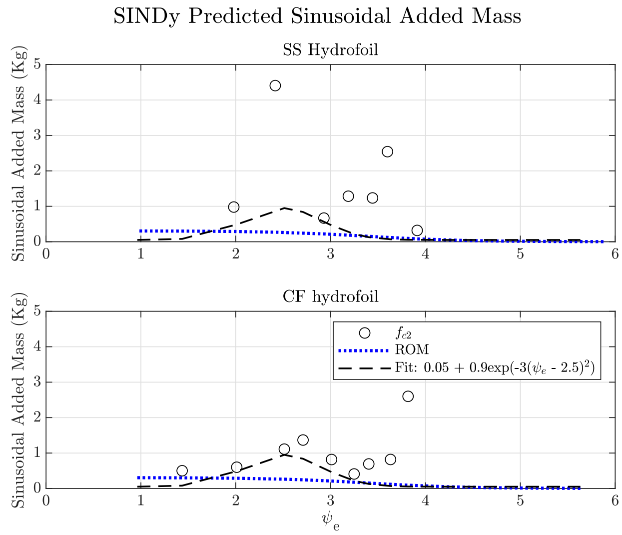

Figure 6: SINDy predicted coefficients of the time-varying sinusoidal fluid added mass. The open black circles denote the amplitudes (square root of the sum of the squares) of the sine and cosine terms in Equation 20 at the Type II cavity shedding frequency. The fit is shown by the black dashed line. Values predicted by SINDy show that time-varying fluid damping is significant in the fluid-structure interaction.

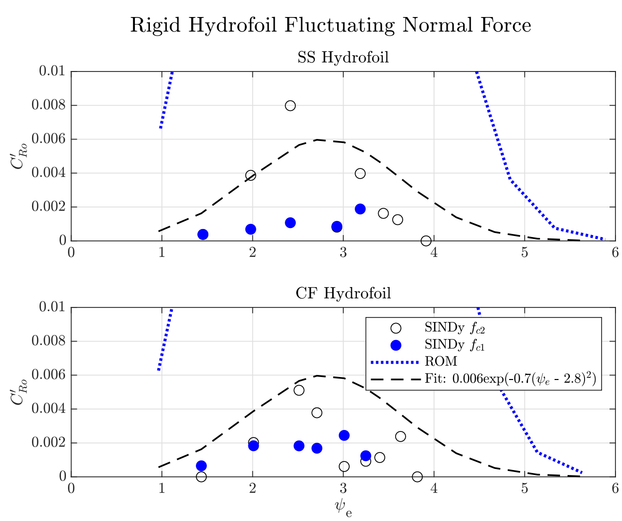

Figure 7: SINDy predicted coefficients of the rigid hydrofoil fluctuating normal force coefficients (C'_{Ro}) compared to ROM values developed by Young et al. (2022). The fit of the SINDy predicted value is shown by the black dashed line. Values predicted by SINDy are an order of magnitude lower compared to the ROM values.

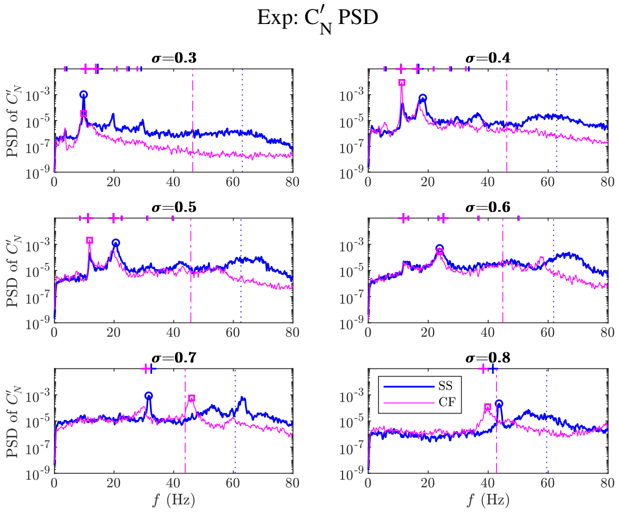

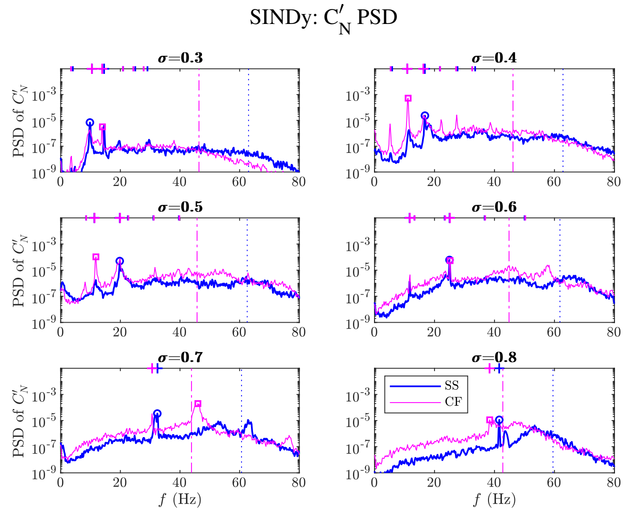

Figure 8: The power spectral densities of the measured C'_N for the SS and the CF hydrofoils are shown with the blue and the magenta line, respectively. The blue circle and magenta square indicate the frequency with the highest magnitude. The vertical dashed lines indicate the system frequency. The crosses on the top axis indicate the cavity shedding frequencies, and the vertical dash markers indicate the heterodyne frequencies.

Figure 9: The power spectral densities of C'_N as recreated by the SINDy data-driven model with the training data. The PSD is shown in the blue line for the SS hydrofoil and shown in the magenta line for the CF hydrofoil. The blue circle and magenta square indicate the frequency with the highest magnitude. The vertical dashed lines indicate the system frequency. The crosses on the top axis indicate the cavity shedding frequencies, and the vertical dash markers indicate the heterodyne frequencies. The signature frequencies compare well with those from the PSDs of the measured C'_N, shown in Figure 8. The PSDs also contain slightly higher noise at higher frequencies due to numerical differentiation, and the magnitude is generally about two orders of magnitude lower than the experimental data.

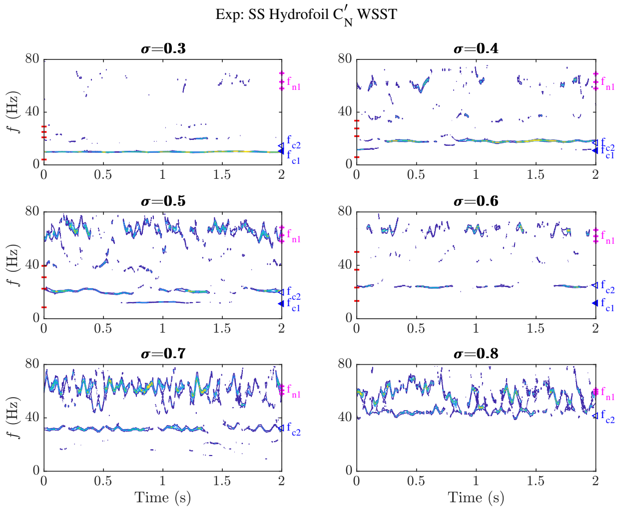

Figure 10: The WSSTs of the measured fluctuating normal force coefficient (C_N') of the SS hydrofoil. The contours shows energy concentration in dB at a given frequency and time. Markers on the right axis indicate the predicted Type I (f_{c1}) and Type II (f_{c2}) cavity shedding frequencies, as well as the predicted system bending frequency (f_{n1}). The red dash markers on the left axis indicate the predicted heterodyne frequencies.

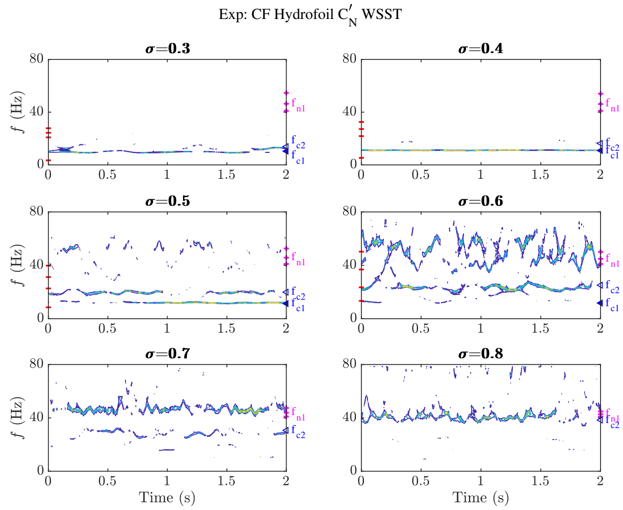

Figure 12: The WSSTs of the fluctuating normal force coefficient (C_N') of the CF hydrofoil. The contours shows energy concentration in dB at a given frequency and time. Markers on the right axis indicate the predicted Type I (f_{c1}) and Type II (f_{c2}) cavity shedding frequencies, as well as the predicted system bending frequency (f_{n1}). The red dash markers on the left axis indicate the predicted heterodyne frequencies.

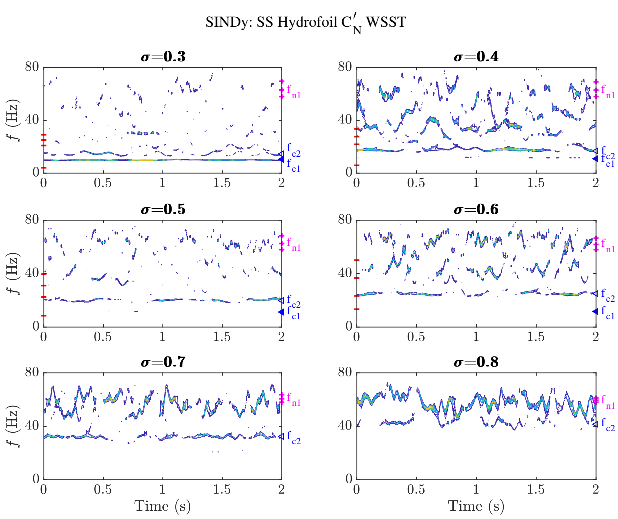

Figure 11: The WSSTs of the measured fluctuating normal force coefficient (C_N') of the SS hydrofoil as reconstructed by SINDy. The contours shows energy concentration in dB at a given frequency and time. Markers on the right axis indicate the predicted Type I (f_{c1}) and Type II (f_{c2}) cavity shedding frequencies, as well as the predicted system bending frequency (f_{n1}). The red dash markers on the left axis indicate the predicted heterodyne frequencies. Good agreement can be seen with the measured WSSTs as shown in Figure 10.

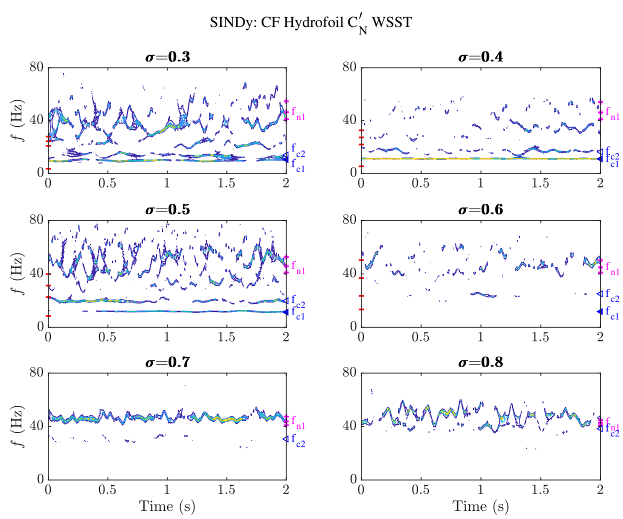

Figure 13: The WSSTs of the fluctuating normal force coefficient (C_N') of the CF hydrofoil as reconstructed by SINDy. The contours shows energy concentration in dB at a given frequency and time. Markers on the right axis indicate the predicted Type I (f_{c1}) and Type II (f_{c2}) cavity shedding frequencies, as well as the predicted system bending frequency (f_{n1}). The red dash markers on the left axis indicate the predicted heterodyne frequencies. Good agreement can be seen with the measured WSSTs shown in Figure 12.

Figures 8 and 9 show good comparison between the dominant frequencies of the measured C_N' and the SINDy reconstructed C_N', including at the cavity shedding frequencies and the system modal frequency. However, the magnitude of the noise comparative to the magnitude of the signature frequencies is higher in the C_N' calculated through the SINDy model when compared to the measured data. This discrepancy is likely due to the noise amplification caused by the differentiation of numerical data, despite applying a bandpass filter throughout the differentiation process. The power of the reconstructed C_N' is also about two orders of magnitude lower when compared to the measured data, likely due to the inaccuracy in the prediction of the rigid hydrofoil forcing. Because the power of C_N' is less than one, the difference of two orders of magnitude in the power of the measured and reconstructed C_N' indicates the difference of one order of magnitude in amplitude. This corresponds to the difference of amplitude between the identified C_{Ro}' and the ROM model presented in Young et al. (2022), as seen in Figure 7.

The results described above can be further observed in wavelet synchrosqueezed transform (WSST) plots, obtained using the algorithm developed by Thakur et al. (2013), of the fluctuating normal force coefficient (C_N'). The WSSTs of the measured C_N' and SINDy model generated C_N' for the SS hydrofoil are shown in Figures 10 and 11, respectively. The WSSTs of the CF hydrofoil can be seen in Figure 12 for the measured data and 13 for the SINDy reconstruction.

It can be seen from the WSSTs that the signature frequencies of C_N' compare well to each other at the cavity shedding frequencies and system modal frequency, although the SINDy model produces higher levels of noise due to the noise amplification of the differentiation process. On the SS hydrofoil in particular, the energy concentrations of the noise can significantly overtake the energy concentrations of the cavity shedding frequencies. It can also be seen in Figures 11 and 13 that the predicted noise content at $\sigma = 0.3$ is particularly high.

Data-Driven Model

After testing the model with the training data, the model was used to generate displacement data. Coefficients identified from both the SS and CF hydrofoils were considered in the curve fitting of the data-driven model. The fitted curves are shown as dashed lines in Figures 3 through 7, and are summarized below in Equations 23 through 27, as well as shown in the legends of Figures 3 through 7. The fitting from Figure 7 is used, even though as previously discussed, the difference of an order of magnitude between the amplitude of the identified C_{Ro}' and the C_{Ro}' predicted in Equation 7 corresponds to that between the modeled and measured C_N'. Thus, the order of magnitude difference between the experimental and predicted displacements is apparent. These fitted equations are used to replace the corresponding terms that are shown in Equation 5, as well as to add the sinusoidal fluid damping term, to write Equation 28. A random time-varying phase angle is assigned to each sinusoidal term to account for the interactions and stochasticity of unsteady cloud cavitation. A random phase angle in time is assigned to the rigid hydrofoil forcing. Predictions are obtained by solving the data-driven model using the Crank-Nicolson method.

$$C_f = 222 \text{ kg/s} \tag{23}$$

$$M_f = 0.92 \text{ kg} \tag{24}$$

$$C_{f,c2} = 0.05 + 100\exp(-2(\psi_e - 2.5)^2) \text{ kg/s} \tag{25}$$

$$M_{f,c2} = 0.05 + 0.9\exp(-3(\psi_e - 2.5)^2) \text{ kg} \tag{26}$$

$$C_{Ro}' = \frac{F_{Ro}'}{qsc} = 0.006\exp\left(-0.7(\psi_e - 2.8)^2\right) \tag{27}$$

$$\begin{aligned} &\left(M_s + M_f + M_{f,c2} sin(2\pi f_{c2} t + \gamma_1(t))\right)\ddot{\delta}' \\ &\quad + \left(C_f + C_{f,c2} sin(2\pi f_{c2} t + \gamma_2(t))\right)\dot{\delta}' \\ &\quad\quad + (K_s)\delta' \\ &= F_{Ro}'(sin(2\pi f_{c1} t + \gamma_3(t)) + sin(2\pi f_{c2} t + \gamma_4(t))) \text{ N} \end{aligned} \tag{28}$$

Figures 14 and 15 compare the spectrograms of the normalized tip bending of the experimental and data-driven model (Equations 23 - 28) results for the SS and CF hydrofoils, respectively.

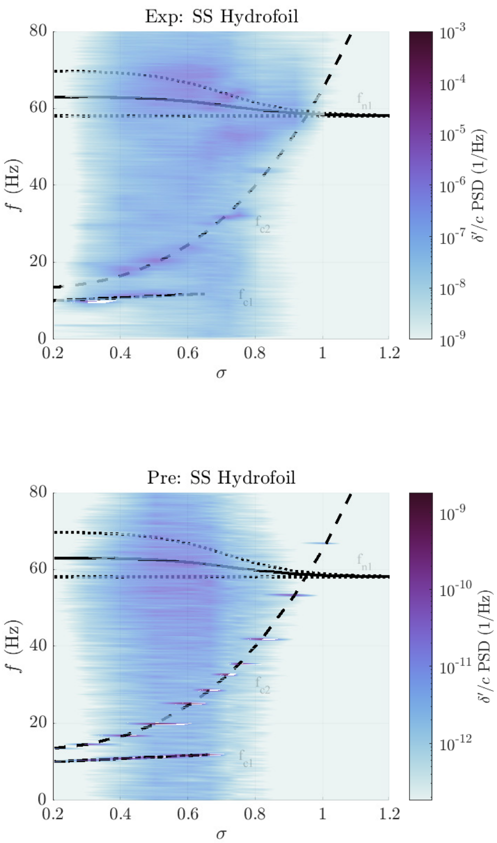

Figure 14: Comparison of the experimental (top) and data-driven model (bottom) spectrograms of the normalized tip bending fluctuations (δ'/c) for the SS hydrofoil. Lines indicating the Type I (f_{c1}) and Type II (f_{c2}) cavity shedding frequencies, as well as the mean and range of variation of the predicted system bending frequency (f_{n1}) are shown in various dashed lines. Lower magnitude is observed on the modeled spectrogram due to the low prediction of rigid hydrofoil forcing. Good general agreement is observed between the two spectrograms for frequency responses, with the predictions showing slightly higher vibrations at areas above the cavity shedding frequencies, but the lock-in is not well captured.

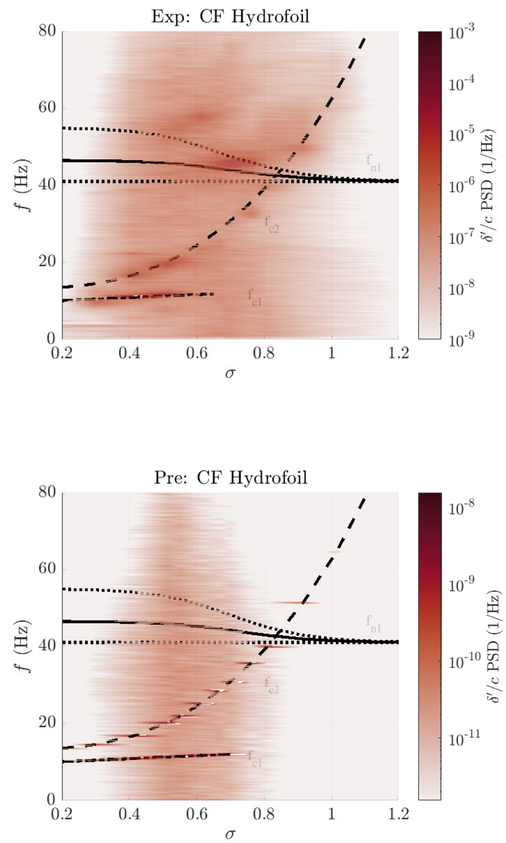

Figure 15: Comparison of the experimental (top) and data-driven model (bottom) spectrograms of the normalized tip bending fluctuations (δ'/c) for the CF hydrofoil. Lines indicating the Type I (f_{c1}) and Type II (f_{c2}) cavity shedding frequencies, as well as the mean and range of variation of the predicted system bending frequency (f_{n1}) are shown in various dashed lines. Lower magnitude is observed on the modeled spectrogram due to the low prediction of rigid hydrofoil forcing. Good general agreement is observed between the two spectrograms for frequency responses, with the predictions showing slightly higher vibration around the cavity shedding frequencies, but the lock-in is not well captured.

It can be seen in Figures 14 and 15 that while the SINDy generated model is generally able to capture cavity shedding frequency activities, it still has trouble modeling lock-in and vibrations at the natural frequency. There is a slight improvement from the ROM presented in Young et al. (2022) in that there is modeling of a broader banded response at the cavity shedding frequencies, which is due to the changes in modeling with the sinusoidal fluid forcing terms. The previously stated discrepancy between the order of magnitudes of the predicted and experimental data can also be seen in Figures 14 and 15.

The difficulties in modeling lock-in can be explained through the composition of the data-driven model. In data-driven modeling, verification of the model would usually be completed with a testing data set not used during model training. However, because of the limitations of time and memory during data collection, the data set is limited to one run per cavitation number at the "Medium" run type, which is suitable for statistical dynamic analysis. Thus, there is no additional experimental data to use for model testing, and hence we compared the predicted coefficients with the ROM values given in Young et al. (2022) in Figures 3 through 7. In addition, when considering Equation 6, the resulting fluctuating normal force is composed mainly of one or two frequencies at the Type II and/or Type I cavity shedding frequencies, with noise added through random phase. Type I and Type II cavity shedding frequencies are each assumed to be a single value with Equations 9 and 10, respectively. However, when observing Figure 8, C_N' contains many frequencies, including at the cavity shedding frequencies, heterodyne frequencies, and system natural frequencies. Type II cavity shedding frequencies also often differ at different points of the span of a hydrofoil (Smith et al., 2020a,b), which is not captured by assuming a single cavity shedding frequency in Equation 10. In other words, the frequency spectrum of the rigid hydrofoil forcing is likely more broadbanded than what Equation 6 captures. Thus, a more reliable estimate of the rigid hydrofoil fluctuating normal force would be necessary to verify the model, which could be obtained through experimental testing of a more rigid model or via numerical simulation of a rigid hydrofoil. In addition, this model was built only considering one set of data per hydrofoil per cavitation number, so if any biases or skews were present in the data, they could not be identified when building the model. A more accurate model could be built if more sets of data were available.

CONCLUSION AND FUTURE WORK

The present work investigated the usage of SINDy to determine a data-driven model that can accurately predict the deformations and normal force of a stiff stainless steel (SS) and a flexible composite (CF) hydrofoil in unsteady cloud cavitation. The model builds upon the form of the physics-based ROM presented in Young et al. (2022), and should be generally applicable for other hydrofoils as long as the structural mass and stiffness properties are known. Cloud cavitation is a form of multiphase flow characterized by periodic cavity growth, shedding, and collapse, which can induce unsteady forces and vibrations, as well as material damage to a structure operating in such flows. There is limited study regarding the physics and governing equations of the FSI of structures in unsteady cloud cavitation. This paper identified the coefficients of the governing nonlinear dynamical system through SINDy and compared the model results to experimental data. SINDy was selected as the machine learning algorithm due to its ability to handle nonlinear terms and its computational efficiency. The SINDy algorithm was only able to be used on a portion of the collected data; at very low and very high cavitation numbers, supercavitation and small partial cavities occur, and the collected data for the deformations and load fluctuations are at the same order of magnitude as noise, which interferes with the identification process.

The SINDy identification showed that the linear fluid inertial and damping terms were in the same order of magnitude as those predicted in the ROM described by Young et al. (2022). Physics informed us that the fluid inertial coefficients should be independent of the material properties since both the SS and CF hydrofoils shared the same undeformed geometry, and fluid damping coefficients should differ slightly due to the system bending frequency. Unlike the ROM presented in Young et al. (2022), the SINDy predicted coefficients were different for the SS and CF hydrofoils. The difference is likely due to the different signal-to-noise ratios of the displacement measurements of the SS and CF hydrofoils, as the SS hydrofoil experienced much lower deformation due to the higher stiffness. As shown in the results, the SINDy algorithm is highly sensitive to noise. The noise amplified during numerical differentiation of polychromatic displacement data for the usage of SINDy likely contaminated the results, despite the filtering and data processing. The SINDy algorithm also showed that not only were linear forcing terms significant to the modeling of FSI in cloud cavitation, fluid damping and inertial forces oscillating at the Type II cavity shedding frequency were also significant. The identified model can accurately capture most of the signature frequencies, such as cavity shedding frequencies and system bending frequencies, from the displacement data, but the intensity of the modeled signature frequencies was often lower than that of the experimental results. The noise at high frequencies from numerical differentiation of the velocity and acceleration from the displacement data likely influenced the coefficients identified by SINDy to amplify signals at lower frequencies and limit signals at higher frequencies.

Verification of the model was completed using numerical data, as there was no new or additional experimental data available for testing. However, the verification is flawed, as the SINDy identification showed that the rigid hydrofoil forcing was not well represented with sinusoidal terms at the cavitation frequency with a random phase. This is demonstrated by the low coefficients identified on the sinusoidal terms corresponding to the rigid hydrofoil forcing. With a rigid hydrofoil forcing term that is highly simplified, it is difficult to capture all of the signature frequencies that occur during cloud cavitation as well as the broadbanded nature of the frequency spectrum. This model predicts tip displacements that display activity at the cavity shedding frequencies and the system modal frequency, but it has difficulty capturing the behavior at other frequencies. As such, it is still difficult to predict phenomena such as nonlinear subharmonic lock-in, where both the force and the displacement are affected. Further experiments using more rigid hydrofoils should be completed to better model the rigid hydrofoil forcing term.

The potential of discovering the governing equations of FSI response in multiphase flow using a hybrid data-driven model is promising, but cavitation is a complex phenomenon, and data regarding a single set of experiments does not produce a complete model applicable to all flexible systems in cavitating flow, especially since there are various types of cavitation that occur on different geometries, materials, and under various operating conditions. To continue in this direction, more data of different systems in cavitating flow should be taken. This work could benefit from additional runs to use both during the model identification phase and model testing phase, and the present model should not be taken as complete. To avoid amplification of noise during the numerical differentiation process, acceleration data should be taken in addition to displacement data during the experimental process. Velocity data could be obtained through integration of the acceleration data instead of differentiation of the displacement data, as numerical integration would smooth the noise rather than amplify it. In addition, because SINDy utilizes least squares modeling, and each identification is done independently of other identifications, it would be beneficial to explore other machine learning algorithms that are more robust when handling time-varying coefficients and can consider for continuity across different sets of data. Multiple models should be built to identify common ground across various systems in cavitating flow, which would better illuminate the physics of multiphase flow. This model could also be expanded to multiple DOFs for more general flexible systems in which material or geometry bend-twist coupling is relevant.

Once the physics and governing equations of cavitation and multiphase flows are better understood, detection and control of cavitation inception will become feasible. With reliable low-fidelity models, displacement and acceleration sensors can be used to monitor flow conditions as well as structural health. If found feasible, building low-fidelity models that can accurately model unsteady multiphase flow, including for free surface applications with unsteady vessel motion, can improve the control authority and safety of autonomous marine vessels.

ACKNOWLEDGEMENTS

Support for this research was provided by the U.S. Office of Naval Research, contract No. N00014-20-C-1099 managed by Dr. Paul Hess. This project was also supported by the Research Training Centre of Naval Design and Manufacturing (RTCNDM), the US Office of Naval Research (Dr. K.-H. Kim, Program Officer) and ONR Global (Dr. W.-M. Lin) through NICOP S&T Grant No. N62909-11-1-7013. The RTCNDM is a University-Industry partnership established under the Australian Research Council (ARC) Industry Transformation grant scheme (ARC ICI40100003). The authors would like to acknowledge the assistance of Mr. S. Kent and Mr. R. Wrigley from the Australian Maritime College for their essential help with setting up and carrying out the experiments.

REFERENCES

Akcabay. D. T. and Young. Y. L. Parametric excitations and lock-in of flexible hydrofoils in two-phase flows. Journal of Fluids and Structures, 57:344–356, 2015. ISSN 0889-9746.

Akcabay. D. T. and Young. Y. L. Steady and dynamic hydroelastic behavior of composite lifting surfaces. Composite Structures, 227:111240, 2019.

Akcabay. D. T. and Young. Y. L. Material anisotropy and sweep effects on the hydroelastic response of lifting surfaces. Composite Structures, 242:112140, 2020.

Akcabay. D. T., Chae. E. J., Young. Y. L., Ducoin. A., and Astolfi. J. A. Cavity induced vibration of flexible hydrofoils. Journal of Fluids and Structures, 49 (Supplement C):463–484, 2014. ISSN 0889-9746. doi: https://doi.org/10.1016/j.jfluidstructs.2014.05.007.

Alavi. S. M., Haddadpour. H., and Firouz-Abadi. R. D. Hydroelastic analysis of two degree of freedom hydrofoil using a reduced-order hydrodynamic model considering unsteady partial sheet cavity flows. Journal of Fluids and Structures, 81:116–130, 2018. ISSN 0889-9746.

Ausoni. P., Farhat. M., Escaler. X., Egusquiza. E., and Avellan. F. Cavitation influence on von Karman vortex shedding and induced hydrofoil vibrations. ASME J. Fluids Eng., 129(8):966–973, 2007. ISSN 0098-2202.

Bhatt. A., Wu. J., Ganesh. H., and Ceccio. S. L. Spatially resolved X-ray void fraction measurements of a cavitating NACA0015 hydrofoil. In 32nd Symposium on Naval Hydrodynamics, 2018.

Blake. W. K. and Maga. L. J. On the flow-excited vibrations of cantilever struts in water. I. Flow-induced damping and vibration. The Journal of the Acoustical Society of America, 57:610, 1975.

Brandner. P. A., Lecoffre. Y., and Walker. G. J. Design considerations in the development of a modern cavitation tunnel. In 16th Australasian Fluid Mechanics Conference, pages 630–637, 2007.

Brandner. P. A., Walker. G. J., Niekamp. P. N., and Anderson. B. An experimental investigation of cloud cavitation about a sphere. Journal of Fluid Mechanics, 656:147–176, 2010.

Brennen. C. E. Cavitation and Bubble Dynamics. Oxford University Press, 1995.

Brunton. S. L., Proctor. J. L., and Kutz. J. N. Discovering governing equations from data by sparse identification of nonlinear dynamical systems. Proceedings of the National Academy of Sciences of the United States of America, 113(15):3932–3937, 2016.

Callenaere. M., Franc. J., Michel. J., and Riondet. M. The cavitation instability induced by the development of a re-entrant jet. Journal of Fluid Mechanics, 444: 223–256, 2001. ISSN 1469-7645.

De La Torre. O., Escaler. X., Egusquiza. E., and Farhat. M. Experimental investigation of added mass effects on a hydrofoil under cavitation conditions. Journal of Fluids and Structures, 39:173–187, 2013.

Fujii. A., Kawakami. D. T., Tsujimoto. Y., and Arndt. R. E. A. Effect of hydrofoil shapes on partial and transitional cavity oscillations. ASME J. Fluids Eng., 129(6):669–673, 2007.

Ganesh. H., Mäkiharju. S. A., and Ceccio. S. L. Bubbly shock propagation as a mechanism for sheet-to-cloud transition of partial cavities. Journal of Fluid Mechanics, 802:37–78, 2016. ISSN 0022-1120.

Ganesh. H., Bhatt. A., and Ceccio. S. L. Influence of tunnel blockage on the partial cavity dynamics of cavitating NACA0015 hydrofoils. In 34th Symposium on Naval Hydrodynamics, 2022.

Gao. C., Zhang. W., Kou. J., Liu. Y., and Ye. Z. Active control of transonic buffet flow. Journal of Fluid Mechanics, 824:312–351, 2017.

Harwood. C., Felli. M., Falchi. M., Ceccio. S. L., and Young. Y. L. The hydroelastic response of a surface-piercing hydrofoil in multiphase flows: Part I - Passive hydroelasticity. Journal of Fluids Mechanics, 881:313–364, 2019.

Harwood. C., Felli. M., Falchi. M., Garg. N., Ceccio. S. L., and Young. Y. L. The hydroelastic response of a surface piercing hydrofoil in multiphase flows: Part II - Modal parameters and generalized fluid forces. Journal of Fluid Mechanics, 884:A3, 2020.

Kato. K., Dan. H., and Matsudaira. Y. Lock-in phenomenon of pitching hydrofoil with cavitation breakdown. JSME International Journal Series B Fluids and Thermal Engineering, 49(3):797–805, 2006.

Kawanami. Y., Kato. H., Yamaguchi. H., Tanimura. M., and Tagaya. Y. Mechanism and control of cloud cavitation. ASME J. Fluids Eng., 119(4):788–794, 1997. ISSN 0098-2202.

Lelong. A., Guiffant. P., and André Astolfi. J. An experimental analysis of the structural response of flexible lightweight hydrofoils in cavitating flow. Journal of Fluids Engineering, 140(2): 021116–021116–9, November 2017. ISSN 0098-2202. doi: 10.1115/1.4037990.

Luo. J. Smooth differentiation, 2022. URL https://www.mathworks.com/matlabcentral/fileexchange/6170-smooth-differentiation.

Náprstek. J. and Fishcer. C. Super and sub-harmonic synchronization in generalized van der Pol oscillator. Computers and Structures, 224:106103, 2019.

Ng. G. W., Vishneek. A. S., Martins. J. R. R. A., and Young. Y. L. Scaling the dynamic response and stability of composite hydrodynamic lifting surfaces. Composite Structures, 285:115148, 2022.

Pham. T. M., Larrarte. F., and Fruman. D. H. Investigation of unsteady sheet cavitation and cloud cavitation mechanisms. ASME J. Fluids Eng., 121(2):289–296, 1999. ISSN 0098-2202.

Phillips. A. W., Cairns. R., Davis. C., Norman. P., Brandner. P. A., Pearce. B. W., and Young. Y. Effect of material design parameters on the forced vibration response of composite hydrofoils in air and in water. In Fifth International Symposium on Marine Propulsors, pages 813–822, 2017a.

Phillips. A. W., Cairns. R., Davis. C., Norman. P., Brandner. P. A., Pearce. B. W., and Young. Y. L. Effect of material design parameters on the forced vibration response of composite hydrofoils in air and in water. In Proceedings of the Fifth International Symposium on Marine Propulsors, 2017b.

Shamsborhan. H., Coutier-Delgosha. O., Caignaert. G., and Nour. F. A. Experimental determination of the speed of sound in cavitating flows. Experiments in Fluids, 49(6):1359–1373, 2010. ISSN 0723-4864.

Smith. S. M., Venning. J. A., Pearce. B. W., Young. Y. L., and Brandner. P. A. The influence of fluid-structure interaction on cloud cavitation about a hydrofoil. part 1. Journal of Fluid Mechanics, 896(A1), 2020a.

Smith. S. M., Venning. J. A., Pearce. B. W., Young. Y. L., and Brandner. P. A. The influence of fluid-structure interaction on cloud cavitation about a hydrofoil part 2. Journal of Fluid Mechanics, 897(A28), 2020b.

Stabile. G., Matthies. H. G., and Borri. C. A novel reduced order model for vortex induced vibrations of long flexible cylinders. Ocean Engineering, 156:191–207, 2018. ISSN 0029-8018.

Thakur. G., Brevdo. E., Fučkar. N. S., and Wu. H. T. The synchrosqueezing algorithm for time-varying spectral analysis: Robustness properties and new paleoclimate applications. Signal Processing, 93(5):1079–1094, 2013.

Wu. J., Ganesh. H., and Ceccio. S. Multimodal partial cavity shedding on a two-dimensional hydrofoil and its relation to the presence of bubbly shocks. Experiments in Fluids, 60(4):66, 2019.

Young. Y. L., Harwood. C. M., Montero. F. M., Ward. J. C., and Ceccio. S. L. Ventilation of lifting bodies: Review of the physics and discussion of scaling effects. Applied Mechanics Reviews, 69(1):010801, 2017.

Young. Y. L., Wright. T., Yoon. H., and Harwood. C. M. Dynamic hydroelastic response of a surface-piercing strut in waves and ventilated flows. Journal of Fluids and Structures, 94:102899, 2020.

Young. Y. L., Chang. J. C., Smith. S. M., Venning. J. A., Pearce. B. W., and Brandner. P. A. The influence of cloud cavitation about a stiff and a flexible hydrofoil. Part 3. Journal of Fluids Mechanics, 934:A2, 2022.

Zarruk. G. A., Brandner. P. A., Pearce. B. W., and Phillips. A. W. Experimental study of the steady fluid-structure interaction of flexible hydrofoils. Journal of Fluids and Structures, 51:326–343, 2014.

DISCUSSION AND AUTHORS' REPLY

We would like to first thank all the reviewers for their time and feedback. The authors' reply are given in italic font after comments presented by each reviewer. The contents of this paper have been revised based on the reviews received.

Dr. Tom J. C. van Terwisga
MARIN / TU Delft, R&D Department, Wageningen, The Netherlands

The authors are to be commended for a high level paper on Fluid Structure Interaction, integrating the complexity of cloud cavitation excitation with the complex structural dynamics of a flexible composite foil.

They are in search of the limitations of data driven structural response models and conclude that the noise level in experimental data, particularly in the cavitation number range where cloud excitation dynamics became less dominant, is too large to come to a reliable prediction of the structural response. Also the relatively simple sinusoidal model that should capture the dynamics of the normal force acting on the foil limits a reliable prediction of the response over a broad frequency range.

But in the end, the purpose of the prediction model determines the required reliability and required resolution in the frequency. And so, the applicability of the current model, with its restrictions in reliability at certain cavitation numbers, might still be adequate for control system design or structural health monitoring. Could the authors comment on acceptance criteria for prediction models? Wouldn't the current model offer a sufficient level of uncertainty in the frequency range of interest?

Authors' response - *Thank you for the positive comments. We agree that given the collected tip displacement data, the model is sufficient for learning the key driving frequencies (cavity shedding frequencies and variations of the system resonance frequency in cavitating conditions), and for the design of controllers to suppress flow induced vibrations. By identifying the key cavity forcing frequencies applied to the hydrofoil, flow condition monitoring is possible as well.*

On the other hand, if the objective of the model is accurate estimation of the amplitude and frequency of the unsteady forcing on the hydrofoils, such as for the prediction of accelerated fatigue of hydrofoils made of different materials, then improvement in the model is desired. Thus, obtaining additional sets of experimental data be taken for both training and verifying of the data driven model is crucial to determining the governing equations of fluid-structure interaction response in multiphase flow.

Specific questions and comments on the text of the paper:

1. Introduction, pg 3: ”However, because the knowledge of the physics is currently limited, it is important to develop the model based on data to correct for outdated assumptions.” - Could you be a bit more specific on the outdated assumptions? This is quite vague.

Authors' response - *Invalid assumptions include assumptions such as potential flow or small displacement of the structure. These are commonly made when forming linear theoretical models of a system. For example, viscous FSI effects, such as changes in the tip vortices and shed vortex dynamics caused by flow-induced bending and twisting deformations, may not be negligible. In this case, the potential flow assumption would not be valid.*

2. Captions with Fig. 14 and 15: ”Good general agreement is observed between the two spectrograms, with the predictions showing slightly higher vibrations at areas above the cavity shedding frequencies, but the lock-in is not well captured.” - It seems to me from the spectrograms that the predictions give a slightly lower vibration level, given the slightly less intense colours in the predictions. My interpretation seems to be confirmed by the conclusions: ”... but the intensity of the modeled signature frequencies was often lower than that of the experimental results.”

Authors' response - *The spectrogram created by the model does show slightly less intense colors due to a couple points. Firstly, when lock-in is not well captured, the amplified displacement during this phenomenon cannot be predicted, which would result in a lower vibration level overall. In addition, the broadbanded nature of the hydrofoil vibration is not well captured due to assumptions regarding the rigid hydrofoil forcing, which would reflect in the spectrogram as less intense colors overall.*